





## Upper troposphere dust belt formation processes vary seasonally and spatially in the Northern Hemisphere

Kang Yang <sup>1,2</sup>, Zhien Wang <sup>1,2</sup>✉, Tao Luo<sup>3</sup>, Xiaohong Liu <sup>4</sup> & Mingxuan Wu <sup>5</sup>

Dust aerosols impact global energy balance substantially by acting as efficient ice nuclei to alter cold cloud properties. However, the estimate of dust indirect effect remains uncertain due to simulating dust distributions poorly and lacking reliable dust observations, especially in the upper-troposphere. Here, we characterize and understand upper-troposphere dust sources and transport with an improved dust dataset derived from A-train satellite lidar and radar measurements and an air parcel trajectory model. The distinct upper-troposphere dust belt over the northern hemisphere has seasonally varying base and top heights of  $3.65 \pm 2.84$  and  $8.35 \pm 1.50$  km above mean sea level and its column loading is strongest during spring (March–April–May). The out-of-phase annual cycles of mid-level dust concentration and westerly wind over source regions control the seasonal upper-tropospheric dust loading variations. African deserts contribute the most (46.3%) to the upper-troposphere dust belt in spring and the synoptic trough is the leading (49%) dust lifting mechanism.

<sup>1</sup>Department of Atmospheric and Oceanic Sciences, University of Colorado, Boulder, CO 80303, USA. <sup>2</sup>Laboratory for Atmospheric and Space Physics, University of Colorado, Boulder, CO 80303, USA. <sup>3</sup>Department of Atmospheric Science, University of Wyoming, Laramie, WY 82071, USA. <sup>4</sup>Department of Atmospheric Sciences, Texas A&M University, College Station, TX 77843, USA. <sup>5</sup>Atmospheric Sciences and Global Change Division, Pacific Northwest National Laboratory, Richland, WA 99354, USA. ✉email: [Zhien.Wang@colorado.edu](mailto:Zhien.Wang@colorado.edu)

Dust aerosols are radiatively important since they not only scatter and absorb both shortwave and longwave radiation directly<sup>1</sup>, but they also act as cloud condensation nuclei (CCN) and ice nucleating particles (INPs) to modify cloud properties<sup>2,3</sup>, thereby indirectly influencing radiation. Previous aircraft measurement campaigns found that dust and metallic particles are the dominant heterogeneous INPs (61%)<sup>3</sup>, which happened for 94% of the sampled cirrus cloud encounters. Overall, it is estimated that global net cloud radiative forcing increases by  $\sim 1 \text{ W m}^{-2}$  for each order of magnitude increase in INP concentrations<sup>3</sup>. Despite their effectiveness to act as INPs and being the most abundant aerosol type by mass<sup>4</sup>, the radiative forcing from dust aerosols remains<sup>5,6</sup> uncertain, due to poorly simulated multi-scale dynamical processes and the resulting vertical dust distribution, as well as associated cloud and precipitation systems<sup>5</sup>.

There are large uncertainties in model simulated global dust distributions as indicated by a large spread within themselves and large discrepancies with observations. Model inter-comparison study indicated that normalized vertical profiles of dust concentration among models differ by a factor of two over North Africa<sup>7</sup>. When compared to Cloud-Aerosol Lidar with Orthogonal Polarization (CALIOP) results, these modeled profiles show much faster decreases with altitude below 6 km, with discrepancies up to 400%<sup>7</sup>, and overestimating dust concentrations in the upper troposphere<sup>8</sup>. Another study showed that over the northwestern Pacific, the modeled extinction is considerably larger than CALIOP by more than a factor of two from middle to upper troposphere<sup>9</sup>. Poorly simulated upper troposphere dust distributions could be due to errors in the model representations of processes related to dust emission, transport, and removal<sup>8</sup>. On the other hand, lacking a reliable dust aerosol distribution dataset, especially in the upper troposphere, makes model evaluation and key process study challenging.

Although ground-based lidar measurements are extensively used to document the vertical distributions of dust aerosol<sup>10–12</sup>, global dust aerosol characterization was not possible until the launch of CALIOP on board Cloud-Aerosol Lidar and Infrared Pathfinder Satellite Observation (CALIPSO) in 2006<sup>13</sup>. CALIOP offers high-resolution vertical profiles of clouds and aerosols globally<sup>14–16</sup>, which have been widely used for global dust studies<sup>17–24</sup>. However, dust aerosol in the upper troposphere has received less attention despite its importance. Integrating CALIOP observations with the simulations of an aerosol transport model found that upper troposphere dust can be transported more than one full circuit around the globe before being removed<sup>25</sup>, but this was a case study and gave no climatological information. Combining CALIOP with a trajectory model analysis of summer dust over the Tibetan Plateau (TP) found that most lower troposphere TP dust came from the Taklimakan Desert<sup>26</sup>, but the limited study period and region offered little value on global dust climate impact analyses. Furthermore, a global study of upper troposphere dust requires an improved dust detection with CALIOP measurements due to the difficulty to discriminate optically thin ice clouds and dust aerosols<sup>14,27–30</sup>. Improvements have been made from CALIPSO version 3<sup>31–34</sup> to version 4<sup>29,30,35</sup> dataset, however, the current CALIPSO standard level 2 V4–20 5 km aerosol layer product still misses middle and upper tropospheric optically thin dust layers (see CALIPSO/CloudSat satellites and the dust dataset in the “Methods” section). Also, improved dust extinction retrievals are needed when dust is mixed with other aerosols.

Here, we use an improved dust layer detection and retrieval dataset (see CALIPSO/CloudSat satellites and the dust dataset in the “Methods” section), which substantially improves optically thin dust layer detections by using nighttime-only measurements

to better detect dust layers with 532 nm perpendicular signals and combined CloudSat radar and CALIOP ice cloud detections and the separation of dust extinction from other external mixing aerosol types by a lidar depolarization method<sup>28,36</sup>. The seasonal variations of northern hemisphere upper troposphere dust belt (UTDB) and associated meteorology patterns are analyzed to identify its strongest column mass loading during March–April–May (MAM) and reveal the processes and mechanisms responsible for the observed strong seasonality. Observations are combined with back trajectory analysis and reanalysis global dynamics to reliably identify the sources and uplift mechanisms of upper troposphere dust and to provide essential guidance for model evaluations and improvements.

## Results

**UTDB and large-scale dynamics.** The concept of the Global Dust Belt (GDB)<sup>37</sup>, which refers to dusty source regions stretching from the west coast of North Africa into Central Asia, was proposed long ago and has a great impact on our understanding of dust distributions<sup>17</sup> along with surface conditions and multi-scale dynamics. Figure 1 shows seasonal global dust extinction (defined as total detected dust extinction divided by total all sky observation numbers, averaged from 2007 to 2009) at different altitude ranges. Besides the traditional GDB over source regions in the low troposphere, there is a noticeable high dust extinction region north of 30°N above 4 km above mean sea level (MSL). This feature stands out above 6 km MSL when dust layers are further detached from dust sources, and is therefore defined as the UTDB, which can also be identified from dust occurrences<sup>36</sup>. Dust extinction over North Africa, Arabian Peninsula and Indian subcontinent between 4 and 6 km MSL is stronger in June–July–August (JJA) than MAM; for Taklimakan Desert and Gobi Desert, dust extinction at this level in JJA is close to that in MAM. But the most prominent UTDB is in MAM. However, this seasonal variability is not captured by models<sup>8</sup>, which indicates that key uplift and transport mechanisms carrying dust from source regions to all around the globe are not properly represented by models.

To explore the seasonal variations of the UTDB, we showed 4–6 km and 6–8 km MSL averaged Modern-Era Retrospective analysis for Research and Applications, Version 2 (MERRA-2)<sup>38</sup> reanalysis wind and retrieved dust extinction<sup>28,36</sup> from CALIOP in Fig. 2 (averaged from 2007 to 2009). The 4–6 km MSL averaged wind (Fig. 2c(i) to c(iv)) shows lower part of the polar jet<sup>39,40</sup> between 30°N and 60°N indicating the strongest in December–January–February (DJF) and the weakest in JJA. Accompanied by this is the subtropical jet stream over North Africa and Asia dust source regions, which is prominent in MAM and DJF but barely exists in JJA. Other than polar jet strengths, polar jet locations (purple solid lines in Fig. 2b(i) to b(iv) and c(i) to c(iv) indicate the jet center latitudes) also vary with seasons. The dust extinction between 4–6 km MSL (Fig. 2d(i) to d(iv)) shows a different seasonality. Over African and Asian dust sources, there are more dust aerosols at this level in JJA than MAM, and substantially fewer in September–October–November (SON) and DJF due to weaker dust emission<sup>8</sup> and vertical transport processes. Obviously, the subtropical jet stream at this altitude could bring dust from source regions to the TP, deflect north, south or over (as red solid and dashed lines in Fig. 2b(i) to b(iv)), uplift, then afflux to the polar jet, which transports globally and form the UTDB (Fig. 2b(i) to b(iv)). The transported dust aerosols spread over the Arctic, which was found to impact polar mixed-phase cloud properties<sup>41</sup>.

The UTDB, which is most prominent in MAM (as in Fig. 2b(i) to b(iv)) and weaker and less extensive in other seasons, is a result of

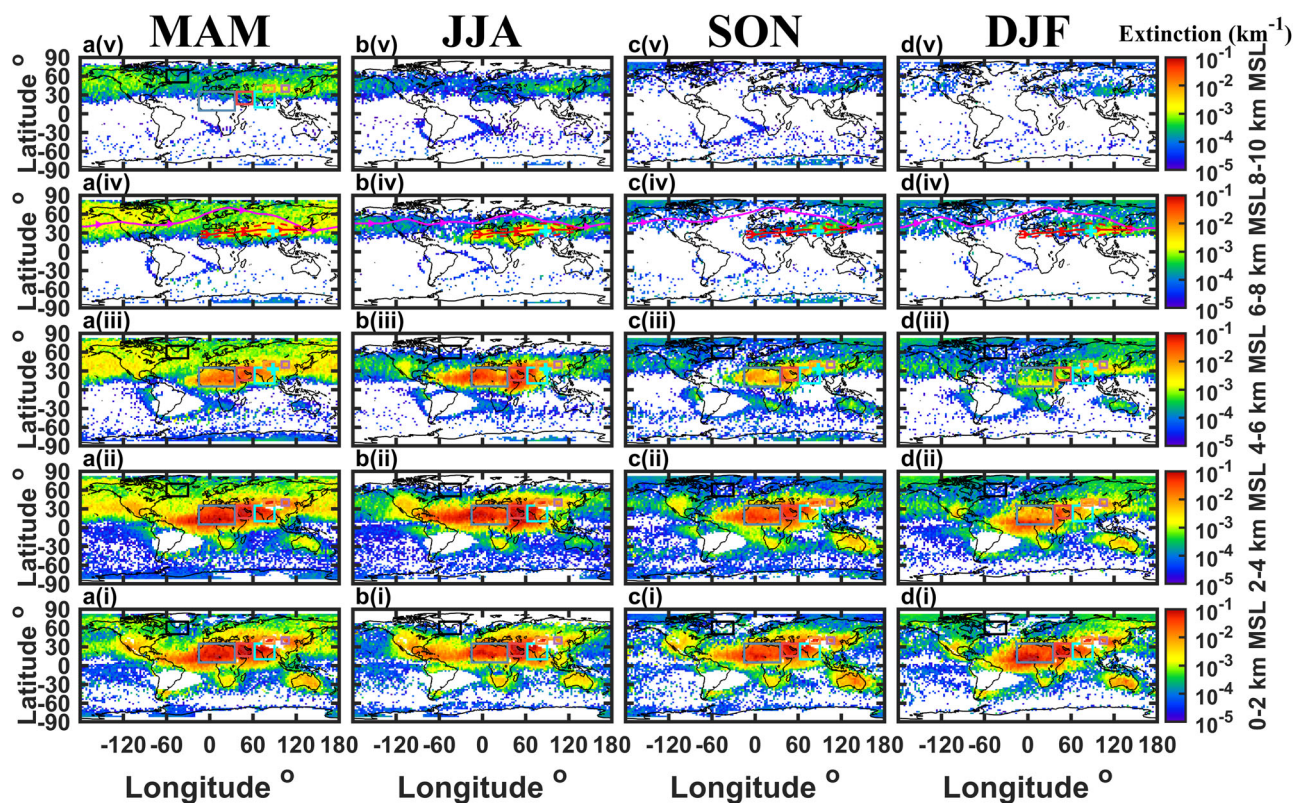


**Fig. 1** Seasonal dust extinction distribution at five height levels. From left to right the four columns (a–d) are four seasons March–April–May (MAM), June–July–August (JJA), September–October–November (SON), and December–January–February (DJF), respectively. From bottom to top the five rows (i–v) are five different levels: 0–2 km, 2–4 km, 4–6 km, 6–8 km, and 8–10 km above mean sea level (MSL). In rows i, ii, iii, and a(v), the five colored boxes indicate five major dust source regions in the northern hemisphere, the black box indicate the “transport region” (–60° to –30° longitude, 50°N–70°N latitude) away from source regions. The cyan plus sign in rows iii and iv marks the location of the Tibetan Plateau (TP). The red and purple lines in row iv are dust transport tracks selected (based on subtropical and polar jet center positions), with small triangles indicating the transport directions. Dust extinction is shown for those pixels with dust occurrence (defined as total detected dust case numbers divided by total all sky observation numbers) larger than 0.01. The white region over South America indicates the South Atlantic Anomaly (SAA) impacted region without reliable dust detection due to high CALIOP noise backgrounds.

the unique combination of the different annual cycles of the westerly jet and 4–6 km MSL dust amount as illustrated in Fig. 3. Northern hemisphere (north of 30°N latitude) averaged upper troposphere column dust mass loading (blue line in Fig. 3b, see Parameter Calculation in the “Methods” section) increases from February and reaches the maximum in MAM, before it starts to dramatically decrease in June and remains below  $0.001 \text{ g m}^{-2}$  from August to December. Meanwhile, MAM column dust mass loading in 2008 is almost twice that in 2007 and 2009, highlighting strong interannual variations. The annual cycles of mid-level (4–6 km MSL) dust mass concentration (derived from retrieved dust extinction coefficient<sup>28,36</sup> by using dust mass extinction efficiency (MEE)<sup>42–44</sup> of  $0.37 \text{ m}^2 \text{ g}^{-1}$  for all seasons<sup>22</sup>, see Parameter Calculation in the “Methods” section) and wind speed over the Africa–West Asia source region have an opposite phase (Fig. 3c). Upper troposphere column dust mass loading reaches its maximum when zonal wind decreases from its peak and mid-level dust mass concentration increases during MAM. To further illustrate this process, mid-level eastward dust mass fluxes from the Africa–West Asia source (red line) and East Asia source (black line) regions are calculated by multiplying dust mass concentration and zonal wind speed (Fig. 3b). To reduce the transported dust impact on local sources, non-elevated high extinction dust profiles were used (see Dust Layer Classification in the “Methods” section, Supplementary Fig. 1 and Supplementary Fig. 2) for eastward flux calculations in the red and black boxes (in Fig. 3a). Clearly, eastward dust mass

fluxes from the two sources are in the same phase as the upper troposphere column dust mass loading, even though there are appreciable interannual magnitude variations. The partial correlation coefficients between the upper troposphere column dust mass loading and mid-level eastward dust mass fluxes for these two sources are 0.72 and 0.33, respectively, which indicated that the Africa–West Asia source region contributes more to the UTDB than the east Asia source region.

To have more insights into the UTDB seasonal variations, longitude-height cross sections of dust extinction along the westerly transport tracks (Fig. 4a(i) to a(iv)) and upper troposphere (above 6 km MSL) vertically integrated dust mass flux divergence<sup>22</sup> (Fig. 4b(i) to b(iv), see Parameter Calculation in the “Methods” section) are shown here. The seasonal variations of dust vertical extent are clear in Fig. 4. For dust layers north of 30°N with top higher than 6 km MSL, all-year dust layer base and top statistics are  $3.65 \pm 2.84$  (base, mean and standard deviation) to  $8.35 \pm 1.50$  km MSL (top). For specific seasons, the base and top heights are  $2.99 \pm 2.44$  to  $8.51 \pm 1.45$  km MSL,  $3.76 \pm 3.27$  to  $8.78 \pm 1.70$  km MSL,  $5.01 \pm 2.93$  to  $8.06 \pm 1.40$  km MSL, and  $4.06 \pm 2.73$  to  $7.75 \pm 1.24$  km MSL for MAM, JJA, SON, and DJF, respectively. In these calculations, if multiple dust layers are detected within one profile, the lowest base and highest top are used for statistics.

In MAM (Fig. 4a(i) and b(i)), starting from North Africa, the subtropical jet stream transports dust eastward and most of them

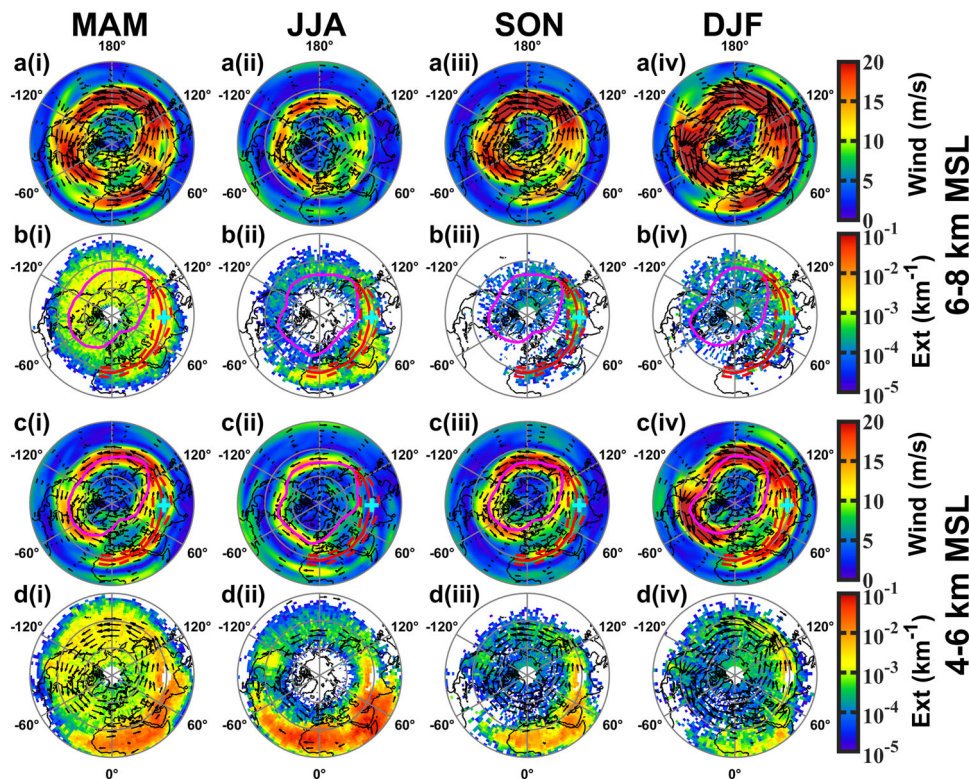


**Fig. 2 Northern hemisphere seasonal horizontal wind and dust extinction (ext) variations between 4–6 km and 6–8 km above mean sea level (MSL).**

For each map, the three circles from outside to inside represent 0°, 30°N, and 60°N latitude. **a(i)–a(iv)** Seasonal mean velocity field overlaid by wind vectors between 6 and 8 km MSL. **b(i)–b(iv)** Seasonal dust extinction between 6 and 8 km MSL. The red and purple lines are dust transport tracks (same as in Fig. 1). **c(i)–c(iv)** Same as **a(i)** to **a(iv)** but for between 4 and 6 km MSL. **d(i)–d(iv)** Seasonal dust extinction overlaid by wind vectors with wind speed larger than 7 m/s between 4 and 6 km MSL. From left to right are four seasons March–April–May (MAM), June–July–August (JJA), September–October–November (SON) and December–January–February (DJF), respectively. The cyan plus sign in rows **b** and **c** marks the location of the Tibetan Plateau (TP). Dust extinction is shown for those pixels with dust occurrence larger than 0.01.

are kept below 6 km MSL west of 10° longitude, then some enter the upper troposphere around 15°–25°. A tremendous amount of dust reaches above 6 km MSL between 30° and 60° on the path toward the TP over the Arabian Peninsula and northern India. Slight upward transport occurs between 60° and 80° as dust aerosols pass over the TP, whereafter they become mixed with some Taklimakan (around 75°–90° longitude) and Gobi desert (around 100°–110° longitude) dust until 120° (Supplementary Fig. 3). East of 120° longitude, the subtropical and polar jets merge and the amount of upper troposphere dust starts to decrease considerably until 160°; meanwhile, dust layers are mainly elevated (see Dust Layer Classification in the “Methods” section, Supplementary Figs. 2 and 3) due to upward motion or strong boundary layer top temperature inversion over the ocean (Supplementary Fig. 3). Between –120° to –60°, the amount of upper troposphere dust further decreases initially and then maintains a stable level over the US, meanwhile non-elevated dust aerosols increase their contributions (Supplementary Fig. 3) due to sinking motions associated with mountains and local dust source contributions in this region. Then, these dust layers transport upwards again east of –60° but have no major impact on the upper troposphere dust. Dust extinction gradually decreases east of –30°, then follows the polar jet to high latitudes and comes back where it approaches Africa–Asia sources around 100° longitude and merges with new dust there to transport around the globe again; sometimes they could also go southward around –30° longitude to incorporate with the subtropical jet over North Africa.

For JJA, although there is plenty of dust at mid-level over North Africa and west Asia sources in Fig. 4a(ii), much fewer dust aerosols are transported east of 60° and lifted, where weak mid-level westerly wind turns northerly. For DJF, the subtropical westerly jet over North Africa and Asia sources is even stronger (Fig. 2c(iv)), but only a small amount of dust aerosols transports into the upper troposphere, since there is limited mid-level dust over North Africa and west Asia sources (Fig. 4a(iv), around –15° to 60° longitude) despite moderate intensity of east Asia sources (Fig. 4a(iv), around 75°–110° longitude). The major uplift region noticeably shifts to northeast India and TP in DJF (Fig. 4b(iv)).

**Upper troposphere dust source and uplift mechanism contributions.** Upper troposphere dust originating from different sources may have different optical properties<sup>45,46</sup> and ice nucleation efficiency<sup>47–49</sup>, thus source contributions need to be evaluated to better determine dust impacts. Meanwhile, mechanisms controlling dust uplift processes are necessary to understand the seasonal variations of the UTDB and improve model representations of related processes to reliably simulate upper troposphere dust distributions and their impacts. Past studies on dust source contributions are either based on specific cases<sup>50–52</sup> or focused on small regions like the TP<sup>26</sup>. Here, we developed a climatology view for the UTDB by combining 3-year CALIOP observations, MERRA-2 reanalysis and Hybrid Single Particle Lagrangian Integrated Trajectory (HYSPPLIT) model analysis<sup>53,54</sup>.

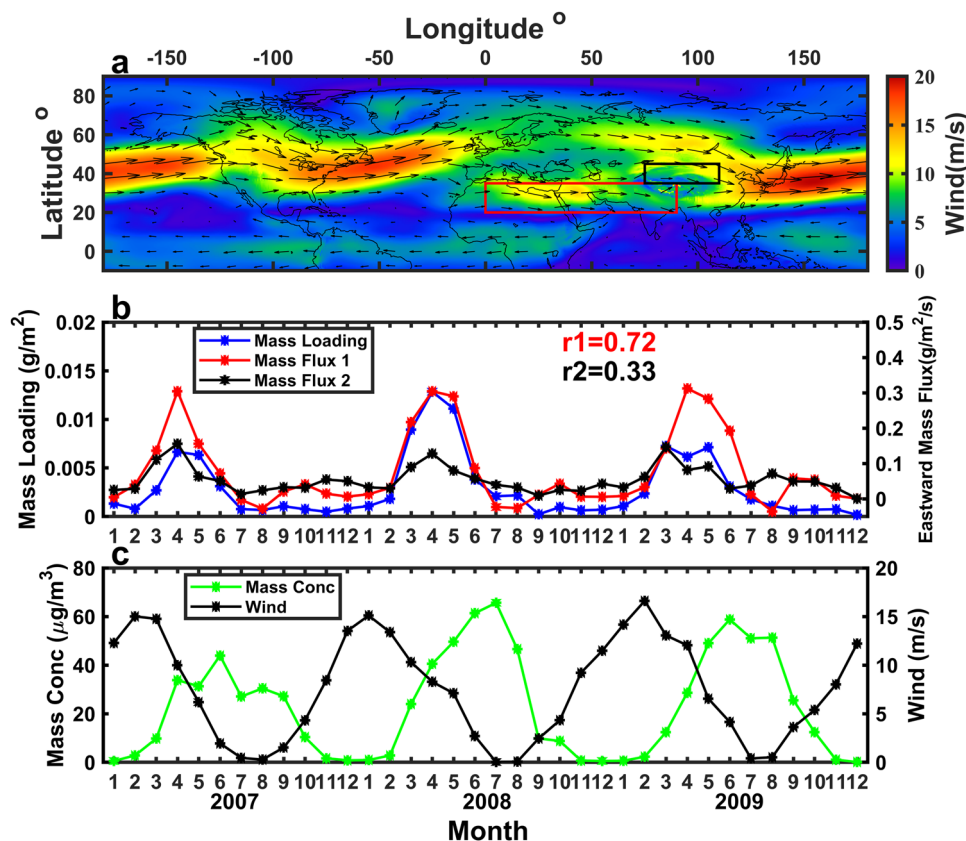


**Fig. 3** The seasonal upper troposphere column (above 6 km above mean sea level (MSL)) dust mass loading, controlled by the seasonal variations of source dust mass concentration (mass conc) and wind. **a** All season averaged velocity field overlaid by wind vectors averaged between 4 and 6 km MSL. The red box ( $0^{\circ}$ – $90^{\circ}$  longitude,  $20^{\circ}$ N– $35^{\circ}$ N latitude) represents major Africa–West Asia dust source regions under the influence of the westerly jet, and the black box ( $75^{\circ}$ – $110^{\circ}$  longitude,  $35^{\circ}$ N– $45^{\circ}$ N latitude) covers East Asia dust source regions. **b** Monthly upper troposphere column dust mass loading (blue line) averaged north of  $30^{\circ}$ N latitude, and monthly eastward dust mass flux averaged between 4 and 6 km MSL in the red box (1) and black box (2). The mass flux 1 (red line) is associated with  $r_1$  and the red box in Fig. 3a, and the mass flux 2 (black line) is associated with  $r_2$  and the black box in Fig. 3a. **c** Monthly dust mass concentration (green line) and zonal wind (black line) averaged between 4 and 6 km MSL in the red box (Fig. 3a).

Before illustrating the climatology results for upper troposphere dust sources and uplift mechanisms, a case is shown (Fig. 5a(i)–a(v)) to briefly introduce the methodology. Upper troposphere dust layers detected by CALIOP at 6.5, 7, 7.5, 8, 8.5, 9, 9.5, and 10 km MSL and horizontally every 50 profiles (around 55 km, Fig. 5a(i)) are selected as starting points for 10-day back trajectory analysis with the HYSPLIT, which is widely used for smoke/dust transport study<sup>23,25,50,55</sup>. The back trajectory height variations are used to determine source regions<sup>26,50,51</sup> (see HYSPLIT model and back trajectory analysis in the “Methods” section). The trajectories in Fig. 5a(ii) and a(iii) show that the uplifting happened over northeast Africa and the Arabian Peninsula, where large trajectory height change was detected, and around 2 to 3 days before the trajectory starting time as highlighted by red circles. Clearly, a deep trough exists over northeast Africa (Fig. 5a(iv)) and strong upward motion is ahead of the trough (as circled in red, Fig. 5a(v)), which supports the height dependent trajectories (Fig. 5a(ii) and a(iii)). Thus, the uplift mechanism (Supplementary Table 1) is classified as the trough lifting.

To produce a reliable UTDB source and uplift mechanism climatology, upper troposphere dust layers within  $30^{\circ}$ N– $90^{\circ}$ N from 2007 to 2009 are used as starting points. Figure 5b(i) to b(iv) and c(i) to c(iv) are based on a total of 65836 back trajectories, which descend to the dust source regions.

In MAM, 46.3% of upper troposphere dust originates from Africa, while the Arabian Peninsula also contributes 37.7% (Fig. 5b(i)). Because some trajectories could go through two

source regions and both sources are counted, the sum of percentages in one season may exceed 100%. In JJA (Fig. 5b(ii)), African contribution considerably decreases, while the Arabian Peninsula and the Taklamakan Desert are the highest two contributors among the five source regions. In SON (Fig. 5b(iii)), the percentage is more evenly distributed among African, Arabian, and Indian sources, with India’s contribution being the highest. The Gobi Desert contribution is 5.9% and inconsequential compared to other sources in SON. Results for DJF (Fig. 5b(iv)) are quite similar to that for MAM, except that Taklimakan contribution is much lower than that in MAM.

For the African source in MAM (Fig. 5c(i)), trough lifting is the leading uplift mechanism associated with a large temperature gradient in the mid-latitude and frequent synoptic cyclone (below upper level trough)<sup>51</sup>. Meanwhile, the trough could work with Zagros Mountain in the northeast Arabian region simultaneously lifting dust (the trough and mountain lifting) or work with the TP subsequently (the trough then mountain lifting). For the Arabian source in JJA (Fig. 5c(ii)), the trough lifting contribution substantially decreases while locally generated increases, since the dry convective process is much more active during this time. For the African source in DJF (Fig. 5c(iv)), the result is quite similar to that in MAM, as they have the most similar large-scale wind patterns (Fig. 2a(i) to a(iv) and c(i) to c(iv)). For the Indian source in SON, the trough and mountain lifting is the dominant mechanism, because upward motion ahead of small troughs could always work together with southwesterly flow toward the TP.

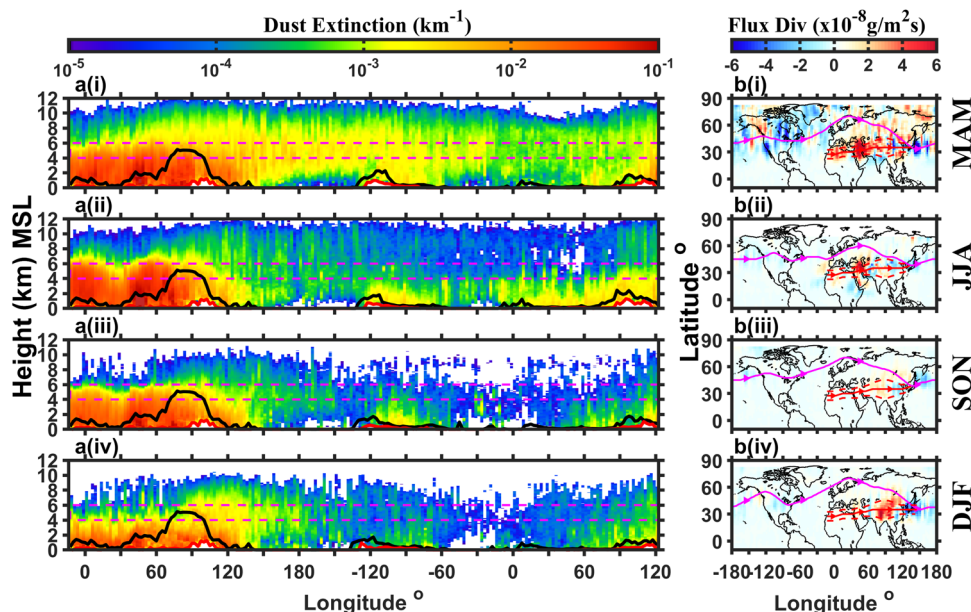


**Fig. 4** Seasonal longitude-height cross sections of dust extinction and upper troposphere (above 6 km above mean sea level (MSL)) vertically integrated dust mass flux divergence (flux div). **a(i)–a(iv)** Longitude-height cross sections of dust extinction along the selected global transport tracks. The dust extinction in **a(i)–a(iv)** is averaged between the red dashed lines (Fig. 4b(i) to b(iv)) from  $-15^\circ$  to about  $135^\circ$  longitudes and after that between  $\pm 5^\circ$  latitude along the purple line. Black and red solid lines in **a(i)–a(iv)** indicate the maximum and minimum terrain heights between the average latitudes along the track. The pink dashed lines indicate 4 and 6 km MSL height respectively. **b(i)–b(iv)** Upper troposphere vertically integrated dust mass flux divergence calculated from CALIOP observations and MERRA-2 reanalysis, red color indicates divergence and upward transport, blue color indicates convergence and downward transport. The red and purple lines are dust transport tracks (same as in Fig. 1 and Fig. 2), with small triangles indicating the transport direction. From top to bottom are four seasons March–April–May (MAM), June–July–August (JJA), September–October–November (SON) and December–January–February (DJF), respectively.

## Discussion

Here, we provide profound insights on upper troposphere dust transport with a height-resolved global dust distribution dataset. Results suggest that dust from Africa and Asia sources could be transported eastward by the subtropical westerly jet and merge with the polar jet stream to transport around the globe to form the UTDB in the northern hemisphere. The maximum upward transport regions switch from the Arabian region during MAM and JJA to the TP region during SON and DJF. The out-of-phase annual cycles of mid-level dust mass concentration and westerly wind over Africa and Asia source regions lead to the strong seasonal UTDB variations. The seasonal decreasing of westerly wind and the seasonal increasing of dust amount at mid-level during MAM result in the MAM maxima of eastward transport of dust over Africa and Asia source regions and column dust loading in the UTDB. HYSPLIT back trajectory analysis shows that African sources contribute the most for the UTDB in MAM, and the synoptic trough lifting is the leading uplift mechanism. These results indicate that different scale dynamics processes control the dust upward and global upper troposphere dust transport other than processes controlling dust emissions in the source regions. The interannual variations of large-scale and local-scale dynamics lead to interannual UTDB variations. Thus, to realistically simulate dust-cloud (ice and mixed-phase) interactions and their radiative impacts, models have to reliably represent these key processes identified here.

## Methods

**CALIPSO/CloudSat satellites and the dust dataset.** CALIPSO and CloudSat, as part of the A-train constellation of satellites, were launched in April 2006 together<sup>56,57</sup>, which gives a 16-day repeat cycle with crossing equator around 13:30 local time<sup>14</sup>. Major instruments onboard CALIPSO include CALIOP<sup>58</sup>, Imaging Infrared Radiometer (IIR), and Wide Field Camera (WFC)<sup>13</sup>. CALIOP level 1B data<sup>35,59</sup> provides attenuated backscatter profiles of aerosols and clouds at three

channels: 532 nm total, 532 nm perpendicular, and 1064 nm total. CALIOP profiles have 30 m vertical and 330 m horizontal resolutions below 8.2 km, and 60 m vertical and 1 km horizontal resolutions up to  $\sim 20$  km. CloudSat carries a 94 GHz cloud profiling radar (CPR) with an instantaneous footprint of approximately  $1.4 \times 2.5$  km (across and along track) and vertically oversampled at 240 m with 125 vertical bins spanning from about  $-5$  to 25 km MSL. The CALIOP is more sensitive to high concentration small particles (liquid clouds and aerosols) than the CPR while the CPR is more sensitive to low concentration large particles (ice clouds and precipitation) than the CALIOP. Therefore, combining CPR and CALIOP measurements provides reliable cloud detections and microphysical retrievals. To facilitate the synergy of the CPR and the CALIOP, CALIOP measurements are collocated to CPR footprints and averaged.

Although lidar linear depolarization ratio (LDR) can be used to effectively separate dust from other types of aerosols, the middle and upper troposphere dust detection is challenged by optically thin cirrus, which has high LDR. To overcome this challenge, we use combined CPR and CALIOP measurements for cloud detection and aerosol/cloud discrimination first. CPR not only can pick up some optically thin cloud layer with a few big ice particles, but also help to confirm whether CALIOP identified geometrically thick layer is a cloud or aerosol layer because ice particles in a geometrically thick layer grows big enough to be detected by CPR<sup>60,61</sup>. Then, dust layer identifications<sup>36</sup> and backscatter coefficient (BSC) retrievals<sup>28</sup> are performed for cloud free measurements. Strong solar background makes daytime upper troposphere dust detection not feasible. CloudSat has satellite battery issues for part of 2010 and 2011 and has operated in the daytime-only mode since summer 2011. Thus, only 3 full-year data (2007–2009) combined CALIOP/CPR nighttime measurements are available for this study, which are enough to quantify general UTDB formation mechanisms, although CALIOP-only nighttime measurements extended over 15 years.

The dust detection and identification method<sup>36</sup> takes advantage of strong dust signals from CALIOP 532 nm perpendicular channel measurements. Because high depolarization ratio of dust particles, dust contributions to CALIOP 532 nm perpendicular channel signals are more prominent than to parallel channel signals, which makes optically thin dust layers easy to be detected during night with 532 nm perpendicular channel measurements. First, peak masks within the 532 nm perpendicular channel profile were identified by a threshold of 4 times of the measured noise (one corresponds to peak and zero corresponds to nonpeak). Then, a  $6 \times 3$  (horizontal  $\times$  vertical, same as the following) moving average was calculated for the peak mask to build the mean peak number as the peak index. Possible dust bin is identified by peak index larger than 0.1 (peak mask set to zero if peak index less than 0.1) and the peak index for clear sky is less than 0.1 (corresponding to approximately two peaks within 18 bins, and this threshold is verified by peak

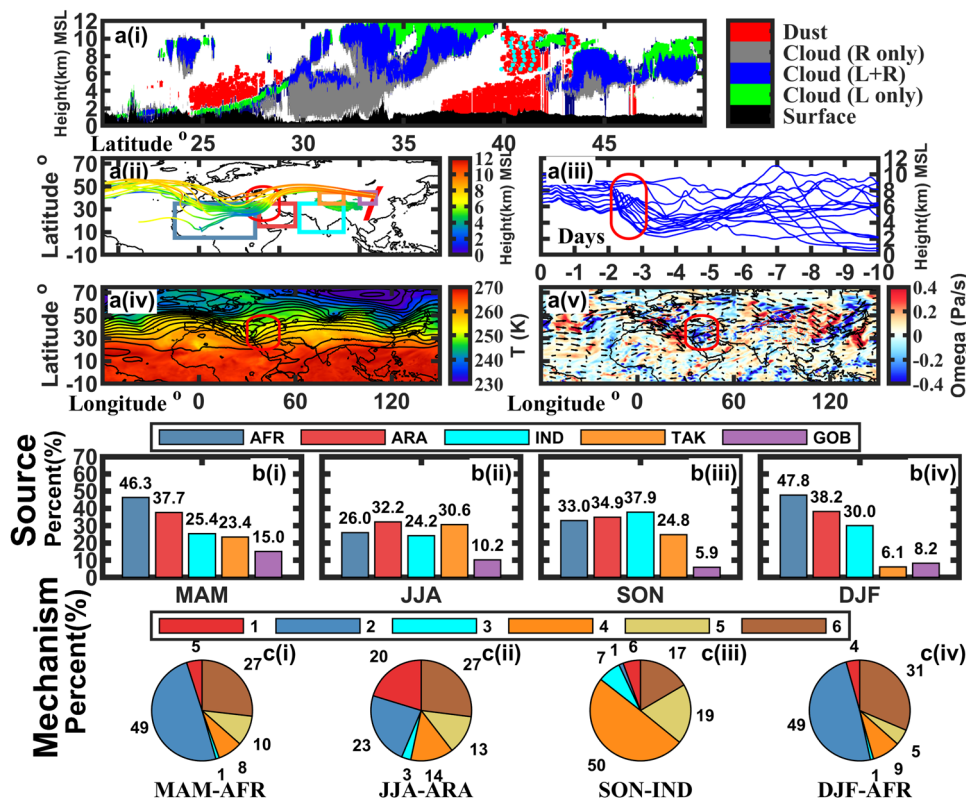


**Fig. 5 Upper troposphere dust source and uplift mechanism analysis: case and climatology.** **a** A CALIPSO case starting from 18:42:50 UTC on March 15, 2008: **a(i)** Identified dust, cloud and surface, in which gray, green, and blue colors represents detected clouds by radar-only (R only), lidar-only (L only) or both (L+R); cyan dots over dust layers between 6–10 km above mean sea level (MSL) around  $\sim 40^\circ\text{N}$  are examples of starting points of back trajectories. **a(ii)** The background color shows the terrain height ( $>4\text{ km}$  only), the bold red line is the CALIOP ground track, the colored lines are the 10-day HYSPLIT back trajectories starting from the cyan dots in **a(i)**, and color represents the height MSL; the red circle highlights where the uplift happens (similar for red circles in **a(iii)–a(v)**). **a(iii)** Back trajectory heights with time (for viewing convenience, only half of the trajectories starting from cyan dots in **a(i)** are shown). **a(iv)** MERRA-2 500 hPa temperature (color fill) overlaid with 500 hPa isoheight (black contours) at 00 UTC March 13, 2008. **a(v)** MERRA-2 500 hPa omega (color fill) overlaid with 500 hPa wind vectors at the same time. **b** seasonal upper troposphere dust belt (UTDB) dust source contributions; AFR (North Africa,  $-15^\circ$  to  $35^\circ$  longitude,  $5^\circ$ – $35^\circ$  latitude), ARA (Arabian Peninsula,  $37.5^\circ$ – $60^\circ$  longitude,  $15^\circ$ – $35^\circ$  latitude), IND (Indian subcontinent  $62.5^\circ$ – $90^\circ$  longitude,  $10^\circ$ – $35^\circ$  latitude), TAK (Taklimakan Desert  $75^\circ$ – $90^\circ$  longitude,  $35^\circ$ – $45^\circ$  latitude), and GOB (Gobi Desert  $100^\circ$ – $110^\circ$  longitude,  $35^\circ$ – $45^\circ$  latitude) dust source regions are shown in **a(ii)** with the same colored boxes. The four seasons are March–April–May (MAM), June–July–August (JJA), September–October–November (SON) and December–January–February (DJF), respectively. **c** Lifting mechanism partitions for the highest contributing source regions each season: 1–6 lifting mechanisms are 1: local lifting, 2: trough lifting, 3: mountain lifting, 4: trough and mountain lifting, 5: trough then mountain lifting, 6: others.

index statistics for bins above 15 km MSL). To detect the boundary of the possible dust layer, a further three-time iterative examining was performed to set any peak mask to zero to further remove random noise spike impacts if the  $11 \times 3$  and  $21 \times 3$  moving averages of the peak mask are smaller than the corresponding thresholds determined from the clear sky (approximately 2 peaks within 33 and 63 bins, respectively). Now, the peak mask corresponds to the quick dust mask. Then the Fernald method<sup>62</sup> was used to retrieve dust extinction from CALIPSO version 4.00 level 1B 532 nm total channel with the dust layer top determined by the quick dust mask; layer mean PDR (LPDR) was then calculated and used to refine the dust mask (LPDR  $< 0.075$  may correspond to other types of aerosols with spherical particles and were removed from the dust mask); finally, dust layers with layer tops below 6 km above ground level (AGL) and extinctions smaller than  $0.02\text{ km}^{-1}$  were removed to avoid classifying optically thin dry sea salt aerosols (entrained from the atmospheric boundary layer and have high depolarization) as dust, and the remaining dust mask (including both pure dust and polluted dust) were regarded as confident ones for further analyses.

The retrieval method<sup>28</sup> solved the single-scattering lidar equation by assuming a mixture of dust and non-dust aerosols with lidar ratio 55 sr for dust and 25 sr for non-dust, and depolarization ratio 0.25 for dust and 0.05 for non-dust aerosols, then separating dust and non-dust contributions by iterative calculation, during which CALIPSO level 1B 532 nm total and perpendicular channels were used. The details could be found in ref. <sup>28</sup>. Dust extinction is calculated from BSC by multiplying the lidar ratio of 55 sr for dust<sup>24,63</sup>. Seasonal global dust extinction is calculated by averaging profiles into  $2.5^\circ \times 2.5^\circ \times 0.06\text{ km}$  boxes.

Seasonal dust occurrence comparison between our data<sup>36</sup> and CALIPSO Level 2 (CAL L2) V4-20 aerosol layer products<sup>29,30</sup> are shown in Supplementary Fig. 4 and

Supplementary Fig. 5. For CAL L2 dust occurrence, the dust cases include both dust and polluted dust with 5, 20, and 80-km horizontal averaging. Meanwhile, cloud-aerosol discrimination score outside  $[-100, -20]$  range are rejected and all samples below 60 m AGL are excluded as suggested by ref. <sup>64</sup>. CALIPSO V4 clearly has noticeable dust layer detection improvements north of  $30^\circ\text{N}$  above 4 km AGL (mainly in MAM) compared with V3 (by comparing Supplementary Fig. 4 with Fig. 3 in ref. <sup>36</sup>). However, compared with our result (Supplementary Fig. 4), CAL L2 V4 still underestimates dust occurrence above 4 km AGL. In MAM, the mean dust occurrence north of  $30^\circ\text{N}$  in our data is 0.25 between 4 and 6 km AGL, 0.18 between 6 and 8 km AGL, and 0.08 between 8 and 10 km AGL, and CAL L2 V4 misses 0.15 (60%), 0.10 (56%), and 0.03 (38%), respectively. This difference could also be observed in Supplementary Fig. 5 where we showed the zonal mean dust occurrence difference (our data–CAL L2 V4). The largest difference is around  $30^\circ\text{N}$  between 2 and 5 km AGL in MAM where most of the African and Asian source regions are, and CAL L2 V4 dust occurrence could be 0.23 (53%) smaller than our data. Above 6 km AGL north of  $30^\circ\text{N}$ , the difference is between 0.04 (38%) and 0.12 (57%) in MAM; while in SON and DJF, the difference is less than 0.01 (40%) in the upper troposphere due to overall low occurrence. Thus, CALIPSO V4 is still not improved enough to present a complete UTDB feature. As discussed above and in ref. <sup>36</sup>, the improvements of the our method are from better optically thin dust layer detections by using nighttime 532 nm perpendicular channel measurements and improved aerosol/cloud separation by combining CALIOP and CloudSat CPR measurements.

Dust detection uncertainties mainly occur from three aspects: The first is the separation of dust from other types of aerosols. We used particle depolarization ratio (PDR) rather than volume depolarization ratio (VDR). VDR is sensitive to

aerosol loading, which makes separating optically thick smoke from optical thin dust difficult (both could have similar VDR). To improve signal-to-noise ratio of PDR calculation, we used LPDR. LPDR was set as  $>0.075$  for the dust layer. With a LPDR threshold of 0.075, 11.8% of dust cases were excluded, while  $\sim 2.7\%$  of non-dust cases could be included, which leads to a net  $\sim 9\%$  underestimation of the dust layer. The algorithm can avoid misclassifying smoke aerosols as dust, as illustrated by Supplementary Fig. 4, no clear upper troposphere dust aerosol detected downwind of southern hemisphere smoke sources (Australia and South Africa). The second is from ice cloud contamination. As indicated above, combined lidar/radar provides reliable aerosol/cloud discriminations and cloud masks, and using PDR can also screen out ice clouds with PDRs higher than dust aerosols. Thus, the algorithm can effectively control optically thin cloud contamination. Based on results in the southern hemisphere, where one would expect low upper troposphere dust, the cloud contamination is less than 0.13%. The third is from missing samples within clouds and below optically thick ice clouds. This bias is true for all aerosol observations with remote sensors. For model and observation comparison studies, we could sample model simulations as observational samplings.

Dust extinction retrieval uncertainties are mainly from two sources: the dust lidar ratio and dust mixing with other aerosol types. A range of dust lidar ratios (from 40 to 70 sr) were reported by ground-based measurements. ref. <sup>65</sup> showed lidar ratios at 523 nm of  $50 \pm 11$  sr for Saharan dust with 10-year observations. With high spectral-resolution lidar (HSRL) and Raman lidar measurements, ref. <sup>66</sup> showed that Asian dust has a mean lidar ratio of 51 sr. Long-range transport leads to removal of coarse mode particles and increase of lidar ratio<sup>67</sup>. Multi-lidar observations<sup>68</sup> of long-range transport of Saharan dust have mean lidar ratios about 60 sr about 2 km AGL. Thus, we used a mean of 55 sr<sup>24,63</sup> in this study for upper troposphere dust with dominated Saharan dust sources, which could lead to  $\sim 10\%$  mean biases assuming the true lidar ratio means within 50–60 sr, but random errors could up to 30% or more. Separating dust contributions from external mixing aerosols depends on assumptions of aerosol depolarizations and lidar ratios. Sensitivity study and comparison with collocated HSRL measurements showed that our CALIOP-based dust extinction retrievals have mean uncertainties less than 20%, although uncertainties for individual profiles could be higher.

**HYSPLIT model and back trajectory analysis.** HYSPLIT trajectories calculated in this study are driven by NCEP/NCAR reanalysis data<sup>69</sup>, with vertical motion using model vertical velocity. The starting points of back trajectories are sampled for CALIOP detected dust layers at 6.5, 7, 7.5, 8, 8.5, 9, 9.5, and 10 km MSL and horizontally every 50 profiles within  $30^{\circ}\text{N}$ – $90^{\circ}\text{N}$  from 2007 to 2009. A total of 202,994 starting points are selected and 10-day back trajectories are run from all these points. Any back trajectories that descend below threshold heights in source regions are determined to originate from the corresponding source. The trajectories are retained for the full 10-day period even after they have their first descents below the threshold height, therefore multiple source regions could potentially be determined from a single trajectory. Source region dependent threshold heights are determined by monthly dust occurrence and BSC cross-sections in those 5 source regions at  $2.5^{\circ} \times 2.5^{\circ}$  horizontal resolution, specifically by picking the lower one between two heights: at which dust occurrence equals 0.3 or BSC equals  $0.00016 \text{ km}^{-1} \text{ sr}^{-1}$ . For those cases, 137,158 (67.57%) trajectories, that the back trajectories keep their heights and never get below the threshold heights in source regions, are assumed to be already lifted for a long period and excluded from the statistics (Fig. 5). Therefore, the source contributions and uplift mechanism statistics are calculated as the number of trajectories below the threshold heights in those five source regions respectively divided by the total number of those trajectories (65,836). Based on our analysis, 33.39% of the back trajectories that have their source regions determined are potentially from multiple source regions.

The general algorithm of the dust uplift mechanism is summarized in Supplementary Table 1. If the starting points of the back trajectories are within the source regions and are classified as non-elevated high extinction ones, these dust aerosols are set to belong to “local lifting”. If part of the back trajectory has a southeasterly shape and its height increases for this region, it is assumed that a trough contributes to this uplift process. If the back trajectory gets over the TP and has its height increased there, it is assumed the mountain (TP) contributes to the uplift process. Whether the trajectory gets lifted over other mountains with terrain height larger than 1.8 km is also considered. The combination of these several characteristics leads to the summarized mechanisms (Supplementary Table 1). The “others” category includes all mechanisms associated with small-scale dynamical processes, which can’t be resolved by the reanalysis dataset.

The HYSPLIT model driven by reanalysis meteorological dataset is widely used for smoke/dust transport study<sup>23,25,50,55</sup>. HYSPLIT has evolved over more than 30 years, and can account for multiple interacting pollutants transported, dispersed, and deposited over local to global scales now. The reliability of HYSPLIT back trajectory depends on reanalysis meteorological data. The NCEP/NCAR reanalysis data captured mesoscale and synoptic-scale dynamics well<sup>69</sup>. Thus, for global dust transport and source identification, statistical results with over 65 thousand samples are reliable to identify major dust source regions resolvable lifting mechanisms (1–5 in Fig. 5c(i)–c(iv)). Because dust lifting events could happen at smaller temporal and spatial scales than those resolved by the reanalysis data, lifting mechanisms for these events can’t be reliably identified and included in the

“others” category, which varies from  $\sim 17$  to 31% for the major source region depending on seasons (see Fig. 5c(i)–c(iv)).

**Dust layer classification.** To better understand dust transport, dust layers are classified into low and high extinction, and elevated and non-elevated layers. To select a suitable extinction threshold, Supplementary Fig. 1 presents the probability distributions of dust layer averaged extinction from source regions and the “transport region”. Based on the distributions for the source and long-range transport regions, using an extinction threshold of  $0.0165 \text{ km}^{-1}$  can identify expected low dust extinction layers in the “transport region” 98% correctly and high extinction dust layers in the source regions 93.36% correctly. Therefore,  $0.0165 \text{ km}^{-1}$  is selected as the dust layer averaged extinction threshold to separate dust layers as high extinction and low extinction ones. Also, dust layers could be separated as elevated and non-elevated ones based on whether their average base heights are above 0.3 km AGL. Combining dust layer extinction and base height, dust layers are separated as non-elevated high extinction ones, non-elevated low extinction ones, elevated high extinction ones and elevated low extinction ones. The MAM global dust distributions of these four groups are shown in Supplementary Fig. 2.

**MERRA-2 data.** MERRA-2 reanalysis data is interpolated to CALIPSO height levels then used in this study except trajectory calculations. In Fig. 2 and Fig. 3,  $0.625^{\circ} \times 0.5^{\circ}$  MERRA-2 wind is converted to  $2.5^{\circ} \times 2.5^{\circ}$  as seasonal dust extinction datasets.

#### Parameter calculation

$$\text{Dust mass concentration} = \frac{\text{dust extinction}}{\text{MEE}} \quad (1)$$

MEE of  $0.37 \text{ m}^2 \text{ g}^{-1}$  is used<sup>22</sup>. Smoothed dust mass concentration is calculated by smoothing the dust mass concentration by a  $11(x) \times 7(y) \times 5(z)$  box, where  $x$  represents the number of grid points of longitude,  $y$  represents the number of grid points of latitude, and  $z$  represents the number of grid points of altitude.

$$\text{Upper troposphere column dust mass loading} = \int_{6\text{km}}^{\infty} \text{dust mass concentration} dz \quad (2)$$

In practice, we use 20 km MSL instead of  $\infty$  as the upper limit of the integral since 20 km MSL is the top of the dust dataset.

$$\text{Eastward Dust mass flux} = \text{smoothed dust mass concentration} * \text{zonal wind speed} \quad (3)$$

$$\text{Dust mass flux divergence} = \frac{\partial(\text{smoothed dust mass concentration} * U)}{\partial x} + \frac{\partial(\text{smoothed dust mass concentration} * V)}{\partial y} \quad (4)$$

where  $U$  and  $V$  is horizontal wind speed from MERRA-2 reanalysis,  $x$  is the distance along the  $U$  direction,  $y$  is the distance along the  $V$  direction.

$$\text{Vertically integrated dust mass flux divergence} = \int_{6\text{km}}^{\infty} \text{dust mass flux divergence} dz. \quad (5)$$

Same upper limit is used as for upper troposphere column dust mass loading.

#### Data availability

The CALIPSO Level 1 and Level 2 data can be obtained from <https://search.earthdata.nasa.gov>. The CloudSat products are available from CloudSat Data Processing Center, <https://www.cloudsat.cira.colostate.edu/>. MERRA-2 data is available at <https://disc.gsfc.nasa.gov/>. Seasonal mean dust extinction and occurrence results presented in this paper are available at <https://doi.org/10.17605/OSF.IO/MRHBV>. The data used directly for generating figures in this article can be found in the Supplementary Data 1.

#### Code availability

The code of the HYSPLIT transport and dispersion model could be obtained from <https://www.ready.noaa.gov>. The code used to analyze the data and the model results in this study is available from the corresponding author upon request.

Received: 28 January 2021; Accepted: 21 January 2022;

Published online: 10 February 2022

#### References

- Chen, S. et al. Modeling the transport and radiative forcing of Taklimakan dust over the Tibetan Plateau: a case study in the summer of 2006. *J. Geophys. Res. Atmos.* **118**, 797–812 (2013).



2. Cziczo, D. J. et al. Clarifying the dominant sources and mechanisms of cirrus cloud formation. *Science* **340**, 1320–1324 (2013).
3. DeMott, P. J. et al. Predicting global atmospheric ice nuclei distributions and their impacts on climate. *Proc. Natl. Acad. Sci. USA* **107**, 11217–11222 (2010).
4. Textor, C. et al. Analysis and quantification of the diversities of aerosol life cycles within AeroCom. *Atmos. Chem. Phys.* **6**, 1777–1813 (2006).
5. Knippertz, P. & Todd, M. C. Mineral dust aerosols over the Sahara: meteorological controls on emission and transport and implications for modeling. *Rev. Geophys.* **50**, RG1007 (2012).
6. Todd, M. C. et al. Quantifying uncertainty in estimates of mineral dust flux: an intercomparison of model performance over the Bodélé Depression, northern Chad. *J. Geophys. Res.* **113**, D24107 (2008).
7. Kim, D. et al. Sources, sinks, and transatlantic transport of North African dust aerosol: a multimodel analysis and comparison with remote sensing data. *J. Geophys. Res. Atmos.* **119**, 6259–6277 (2014).
8. Wu, M. et al. Modeling dust in East Asia by CESM and sources of biases. *J. Geophys. Res. Atmos.* **124**, 8043–8064 (2019).
9. Yu, H. et al. Global view of aerosol vertical distributions from CALIPSO lidar measurements and GOCART simulations: regional and seasonal variations. *J. Geophys. Res.* **115**, D00H30 (2010).
10. Murayama, T. et al. Ground-based network observation of Asian dust events of April 1998 in east Asia. *J. Geophys. Res. Atmos.* **106**, 18345–18359 (2001).
11. Tesche, M. et al. Ground-based validation of CALIPSO observations of dust and smoke in the Cape Verde region. *J. Geophys. Res. Atmos.* **118**, 2889–2902 (2013).
12. Zhang, Z. et al. Three-year continuous observation of pure and polluted dust aerosols over northwest china using the ground-based lidar and sun photometer data. *J. Geophys. Res. Atmos.* **124**, 1118–1131 (2019).
13. Winker, D. M. et al. The CALIPSO mission. *Bull. Am. Meteorol. Soc.* **91**, 1211–1230 (2010).
14. Winker, D. M. et al. Overview of the CALIPSO mission and CALIOP data processing algorithms. *J. Atmos. Ocean. Technol.* **26**, 2310–2323 (2009).
15. Vaughan, M. A. et al. Fully automated detection of cloud and aerosol layers in the CALIPSO lidar measurements. *J. Atmos. Ocean. Technol.* **26**, 2034–2050 (2009).
16. Liu, Z. et al. The CALIPSO lidar cloud and aerosol discrimination: version 2 algorithm and initial assessment of performance. *J. Atmos. Ocean. Technol.* **26**, 1198–1213 (2009).
17. Liu, D., Wang, Z., Liu, Z., Winker, D. & Trepte, C. A height resolved global view of dust aerosols from the first year CALIPSO lidar measurements. *J. Geophys. Res.* **113**, D16214 (2008).
18. Liu, Z. et al. Airborne dust distributions over the Tibetan Plateau and surrounding areas derived from the first year of CALIPSO lidar observations. *Atmos. Chem. Phys.* **8**, 5045–5060 (2008).
19. Huang, J. et al. CALIPSO inferred most probable heights of global dust and smoke layers. *J. Geophys. Res. Atmos.* **120**, 5085–5100 (2015).
20. Uno, I. et al. 3D structure of Asian dust transport revealed by CALIPSO lidar and a 4DVAR dust model. *Geophys. Res. Lett.* **35**, L06803 (2008).
21. Eguchi, K. et al. Trans-pacific dust transport: integrated analysis of NASA/CALIPSO and a global aerosol transport model. *Atmos. Chem. Phys.* **9**, 3137–3145 (2009).
22. Yu, H. et al. Quantification of trans-Atlantic dust transport from seven-year (2007–2013) record of CALIPSO lidar measurements. *Remote Sens. Environ.* **159**, 232–249 (2015).
23. Huang, J. et al. Long-range transport and vertical structure of Asian dust from CALIPSO and surface measurements during PACDEX. *J. Geophys. Res.* **113**, D23212 (2008).
24. Schuster, G. L. et al. Comparison of CALIPSO aerosol optical depth retrievals to AERONET measurements, and a climatology for the lidar ratio of dust. *Atmos. Chem. Phys.* **12**, 7431–7452 (2012).
25. Uno, I. et al. Asian dust transported one full circuit around the globe. *Nat. Geosci.* **2**, 557–560 (2009).
26. Jia, R., Liu, Y., Chen, B., Zhang, Z. & Huang, J. Source and transportation of summer dust over the Tibetan Plateau. *Atmos. Environ.* **123**, 210–219 (2015).
27. Omar, A. H. et al. The CALIPSO automated aerosol classification and lidar ratio selection algorithm. *J. Atmos. Ocean. Technol.* **26**, 1994–2014 (2009).
28. Luo, T. et al. Vertically resolved separation of dust and other aerosol types by a new lidar depolarization method. *Opt. Express* **23**, 14095 (2015).
29. Liu, Z. et al. Discriminating between clouds and aerosols in the CALIOP version 4.1 data products. *Atmos. Meas. Tech.* **12**, 703–734 (2019).
30. Kim, M.-H. et al. The CALIPSO version 4 automated aerosol classification and lidar ratio selection algorithm. *Atmos. Meas. Tech.* **11**, 6107–6135 (2018).
31. Kim, M.-H. et al. Quantifying the low bias of CALIPSO's column aerosol optical depth due to undetected aerosol layers. *J. Geophys. Res. Atmos.* **122**, 1098–1113 (2017).
32. Thorsen, T. J., Ferrare, R. A., Hostetler, C. A., Vaughan, M. A. & Fu, Q. The impact of lidar detection sensitivity on assessing aerosol direct radiative effects. *Geophys. Res. Lett.* **44**, 9059–9067 (2017).
33. Toth, T. D. et al. Minimum aerosol layer detection sensitivities and their subsequent impacts on aerosol optical thickness retrievals in CALIPSO level 2 data products. *Atmos. Meas. Tech.* **11**, 499–514 (2018).
34. Watson-Parris, D. et al. On the limits of CALIOP for constraining modeled free tropospheric aerosol. *Geophys. Res. Lett.* **45**, 9260–9266 (2018).
35. Kar, J. et al. CALIPSO lidar calibration at 532 nm: version 4 nighttime algorithm. *Atmos. Meas. Tech.* **11**, 1459–1479 (2018).
36. Luo, T. et al. Global dust distribution from improved thin dust layer detection using a—train satellite lidar observations. *Geophys. Res. Lett.* **42**, 620–628 (2015).
37. Prospero, J. M. Environmental characterization of global sources of atmospheric soil dust identified with the NIMBUS 7 Total Ozone Mapping Spectrometer (TOMS) absorbing aerosol product. *Rev. Geophys.* **40**, 1002 (2002).
38. Gelaro, R. et al. The modern-era retrospective analysis for research and applications, version 2 (MERRA-2). *J. Clim.* **30**, 5419–5454 (2017).
39. Kidston, J., Frierson, D. M. W., Renwick, J. A. & Vallis, G. K. Observations, simulations, and dynamics of jet stream variability and annular modes. *J. Clim.* **23**, 6186–6199 (2010).
40. Krishnamurti, T. N. The subtropical jet stream of winter. *J. Meteorol.* **18**, 172–191 (1961).
41. Zhang, D. et al. Ice particle production in mid-level stratiform mixed-phase clouds observed with collocated A—train measurements. *Atmos. Chem. Phys.* **18**, 4317–4327 (2018).
42. Li-Jones, X., Maring, H. B. & Prospero, J. M. Effect of relative humidity on light scattering by mineral dust aerosol as measured in the marine boundary layer over the tropical Atlantic Ocean. *J. Geophys. Res. Atmos.* **103**, 31113–31121 (1998).
43. Carrico, C. M. Mixtures of pollution, dust, sea salt, and volcanic aerosol during ACE-Asia: Radiative properties as a function of relative humidity. *J. Geophys. Res.* **108**, 8650 (2003).
44. Denjean, C. et al. Long-range transport across the Atlantic in summertime does not enhance the hygroscopicity of African mineral dust. *Geophys. Res. Lett.* **42**, 7835–7843 (2015).
45. Hofer, J. et al. Optical properties of Central Asian aerosol relevant for spaceborne lidar applications and aerosol typing at 355 and 532 nm. *Atmos. Chem. Phys.* **20**, 9265–9280 (2020).
46. Kim, M.-H., Kim, S.-W. & Omar, A. H. Dust lidar ratios retrieved from the CALIOP measurements using the MODIS AOD as a constraint. *Remote Sens.* **12**, 251 (2020).
47. Krueger, B. J., Grassian, V. H., Cowin, J. P. & Laskin, A. Heterogeneous chemistry of individual mineral dust particles from different dust source regions: the importance of particle mineralogy. *Atmos. Environ.* **38**, 6253–6261 (2004).
48. Hoose, C. & Möhler, O. Heterogeneous ice nucleation on atmospheric aerosols: a review of results from laboratory experiments. *Atmos. Chem. Phys.* **12**, 9817–9854 (2012).
49. Steinke, I. et al. Ice nucleation activity of agricultural soil dust aerosols from Mongolia, Argentina, and Germany. *J. Geophys. Res. Atmos.* **121**(13), 559–13,576 (2016).
50. Creamean, J. M. et al. Dust and biological aerosols from the Sahara and Asia influence precipitation in the western U.S. *Science* **339**, 1572–1578 (2013).
51. Hsu, S.-C. et al. Dust transport from non-East Asian sources to the North Pacific. *Geophys. Res. Lett.* **39**, L12804 (2012).
52. Sugimoto, N., Jin, Y., Shimizu, A., Nishizawa, T. & Yumimoto, K. Transport of Mineral Dust from Africa and Middle East to East Asia Observed with the Lidar Network (AD-Net). *SOLA* **15**, 257–261 (2019).
53. Stein, A. F. et al. NOAA's HYSPLIT atmospheric transport and dispersion modeling system. *Bull. Am. Meteorol. Soc.* **96**, 2059–2077 (2015).
54. Rolph, G., Stein, A. & Stunder, B. Real-time environmental applications and display system: READY. *Environ. Model. Softw.* **95**, 210–228 (2017).
55. McGowan, H. & Clark, A. Identification of dust transport pathways from Lake Eyre, Australia using Hysplit. *Atmos. Environ.* **42**, 6915–6925 (2008).
56. Stephens, G. L. et al. THE cloudsat mission and the A-train: a new dimension of space-based observations of clouds and precipitation. *Bull. Am. Meteorol. Soc.* **83**, 1771–1790 (2002).
57. Stephens, G. L. et al. CloudSat mission: performance and early science after the first year of operation. *J. Geophys. Res.* **113**, D00A18 (2008).
58. Hunt, W. H. et al. CALIPSO lidar description and performance assessment. *J. Atmos. Ocean. Technol.* **26**, 1214–1228 (2009).
59. Vaughan, M. et al. CALIPSO lidar calibration at 1064 nm: version 4 algorithm. *Atmos. Meas. Tech.* **12**, 51–82 (2019).
60. Zhang, D., Wang, Z. & Liu, D. A global view of midlevel liquid-layer topped stratiform cloud distribution and phase partition from CALIPSO and CloudSat measurements. *J. Geophys. Res.* **115**, D00H13 (2010).
61. Zhang, D. et al. Quantifying the impact of dust on heterogeneous ice generation in midlevel supercooled stratiform clouds. *Geophys. Res. Lett.* **39**, 1–6 (2012).
62. Fernald, F. G. Analysis of atmospheric lidar observations: some comments. *Appl. Opt.* **23**, 652 (1984).

63. Groß, S. et al. Optical properties of long-range transported Saharan dust over Barbados as measured by dual-wavelength depolarization Raman lidar measurements. *Atmos. Chem. Phys.* **15**, 11067–11080 (2015).
64. Tackett, J. L. et al. CALIPSO lidar level 3 aerosol profile product: version 3 algorithm design. *Atmos. Meas. Tech.* **11**, 4129–4152 (2018).
65. Berjón, A. et al. A 10-year characterization of the Saharan Air Layer lidar ratio in the subtropical North Atlantic. *Atmos. Chem. Phys.* **19**, 6331–6349 (2019).
66. Liu, Z., Sugimoto, N. & Murayama, T. Extinction-to-backscatter ratio of Asian dust observed with high-spectral-resolution lidar and Raman lidar. *Appl. Opt.* **41**, 2760 (2002).
67. Mattis, I., Ansmann, A., Müller, D., Wandinger, U. & Althausen, D. Dual-wavelength Raman lidar observations of the extinction-to-backscatter ratio of Saharan dust. *Geophys. Res. Lett.* **29**, 20-1-20-4 (2002).
68. Ansmann, A. et al. Long-range transport of Saharan dust to northern Europe: the 11–16 October 2001 outbreak observed with EARLINET. *J. Geophys. Res. Atmos.* **108**, n/a-n/a (2003).
69. Kalnay, E. et al. The NCEP/NCAR 40-year reanalysis project. *Bull. Am. Meteorol. Soc.* **77**, 437–471 (1996).

## Acknowledgements

This work is supported by NASA CloudSat and CALIPSO Science Program (grant NNX16AO94G), NASA The Science of TERRA, AQUA, and SUOMI NPP program (grant 80NSSC19K0299) and NASA grant NNX13AQ41G. Mingxuan Wu is also supported by the US Department of Energy (DOE), Office of Biological and Environmental Research, Earth and Environmental System Modeling program as part of the Energy Exascale Earth System Model (E3SM) project. The Pacific Northwest National Laboratory (PNNL) is operated for DOE by the Battelle Memorial Institute under contract DE-AC05-76RLO1830. We thank the CloudSat team and CALIPSO team for providing data. We gratefully acknowledge the NOAA Air Resources Laboratory (ARL) for the provision of the HYSPLIT transport and dispersion model and/or READY website (<https://www.ready.noaa.gov>) used in this publication. We also acknowledge the Global Modeling and Assimilation Office (GMAO) at NASA Goddard Space Flight Center for the MERRA-2 data. We also thank Brennan Dettmann for his help with the paper.

## Author contributions

K.Y. and Z.W. conceived the principal idea, carried out the analysis and led the role in writing of the manuscripts. T.L., X.L., and M.W. contributed to the interpretation of the results and the writing of the manuscript.

## Competing interests

The authors declare no competing interests.

## Additional information

**Supplementary information** The online version contains supplementary material available at <https://doi.org/10.1038/s43247-022-00353-5>.

**Correspondence** and requests for materials should be addressed to Zhien Wang.

**Peer review information** *Communications Earth & Environment* thanks Zhibo Zhang and the other, anonymous, reviewer(s) for their contribution to the peer review of this work. Primary Handling Editors: Yinon Rudich and Clare Davis. Peer reviewer reports are available.

**Reprints and permission information** is available at <http://www.nature.com/reprints>

**Publisher's note** Springer Nature remains neutral with regard to jurisdictional claims in published maps and institutional affiliations.



**Open Access** This article is licensed under a Creative Commons Attribution 4.0 International License, which permits use, sharing, adaptation, distribution and reproduction in any medium or format, as long as you give appropriate credit to the original author(s) and the source, provide a link to the Creative Commons license, and indicate if changes were made. The images or other third party material in this article are included in the article's Creative Commons license, unless indicated otherwise in a credit line to the material. If material is not included in the article's Creative Commons license and your intended use is not permitted by statutory regulation or exceeds the permitted use, you will need to obtain permission directly from the copyright holder. To view a copy of this license, visit <http://creativecommons.org/licenses/by/4.0/>.

© The Author(s) 2022